

---

# Jets in Active Galactic Nuclei

Alan P. Marscher

Institute for Astrophysical Research, Boston University, 725 Commonwealth Ave.,  
Boston, MA 02215, USA [marscher@bu.edu](mailto:marscher@bu.edu)

**Summary.** The jets of active galactic nuclei can carry a large fraction of the accreted power of the black-hole system into interstellar and even extragalactic space. They radiate profusely from radio to X-ray and  $\gamma$ -ray frequencies. In the most extreme cases, the outward flow speeds correspond to high Lorentz factors that can reach 40 or more. This chapter displays images at various wavebands as well as light curves and continuum spectra that illustrate the variability with location, time, and frequency of the emission from compact, parsec- and subparsec-scale jets. It presents a physical framework for investigating many aspects of the structure and dynamical processes from such data.

## 1 Introduction

Since accretion onto stellar-mass black holes is often accompanied by a pair of jets emanating from the rotational poles, we have the right to expect an even more spectacular brand of jets in active galactic nuclei (AGN). Indeed, AGN jets were the first to be observed. These systems, with their supermassive black holes of millions to billions of solar masses, can produce ultraluminous jets that bore their way through the interstellar medium and into intergalactic space, ending in huge, billowy lobes punctuated by hotspots. Even the less luminous versions disturb the gas in their host galaxies. During the epoch of galaxy formation, this may have controlled the infall of gas so that the central black hole and galactic bulge grew in step with each other.

The wide variety of AGN is reflected in the diversity of their jets. These range from relatively slow, weak, and poorly collimated flows in Seyfert galaxies to strong jets with relativistic speeds in Fanaroff-Riley (FR) I radio galaxies and BL Lacertae (BL Lac) objects to the most luminous, highly focused, and relativistic beams in FR II radio galaxies and radio-loud quasars. The reason for this dichotomy is unclear, although it probably relates to the galactic environment, with Seyfert galaxies usually of spiral morphology, FR I sources hosted by giant elliptical galaxies in rich clusters, and FR II objects in elliptical galaxies lying in somewhat less dense groupings. This might influence the rate of accretion of gas or spin of the black hole, one (or both) of which could be the factor that determines how fast and well-focused an outflow is propelled in the two polar directions.

The most extreme jets with highly relativistic flow velocities are in fact the best-studied variety. This is because relativistic beaming of the radiation amplifies the brightness of these jets so that they can be prominent even at relatively low luminosities if one of the jets points within several degrees of the line of sight. Emission from the jet often dominates the spectral energy distribution of the source in this case, so that observations across the electromagnetic spectrum serve to define the properties of the jet. For this reason, and because one often learns the most by studying extreme cosmic phenomena, this chapter will emphasize relativistic jets pointing nearly at us. AGN with such jets are termed “blazars.”

Because of space limitations, this chapter discusses only a fraction of the phenomenology and physics of AGN jets. The interested reader should consult other sources of information, especially [6, 35, 48, 24].

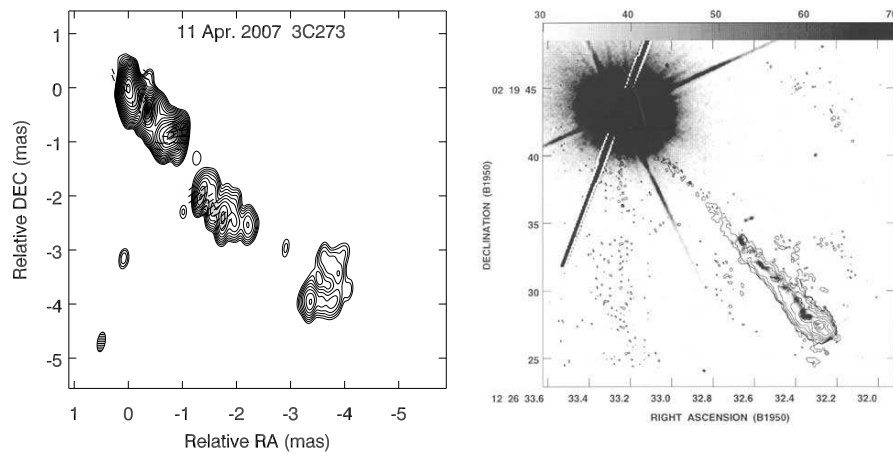


**Fig. 1.** Example of an AGN jet, in the quasar 3C 273. **(Left)** on parsec scales at radio frequency 43 GHz; **(right)** on kiloparsec scales at radio frequency 1.7 GHz (contours) and optical wavelengths centered on 606 nm (greyscale). The core (brightest feature, at the northeast end) of the parsec-scale jet is located very close to the center of the overexposed nucleus in the upper-left corner of the right-hand panel. The scale of the image on the right is 4000 times larger than that on the left. Contours of the radio images in this and subsequent figures are in increments of a factor of 2. At the redshift of 0.158,  $1'' = 2.7$  kpc. **Left:** author’s image, derived from data obtained with the Very Long Baseline Array (VLBA); **right:** from [4], from data obtained with the NASA’s Chandra X-ray Observatory and the Very Large Array (VLA). The VLBA and VLA are instruments of the National Radio Astronomy Observatory, a facility of the National Science Foundation operated under cooperative agreement by Associated Universities, Inc.

## 2 Observed Properties of Jets

The jets of blazars are indeed extreme, with kinetic powers that can exceed the luminosities of entire galaxies and with flow speeds sometimes greater than  $0.999c$ . This section contains a brief overview of the characteristics of jets compiled from a wealth of imaging, spectral, and multiwaveband monitoring and polarization data. Subsequent sections will examine these properties in more detail from a physical standpoint.

### 2.1 Images at Different Wavebands

Figure 1 shows an example of a jet on both parsec and kiloparsec scales, while Figure 2 compares the X-ray and radio emission from a jet on kiloparsec scales. The jet, which broadens with distance from the nucleus, is defined by knots of emission. There is an overall likeness on the different scales, which indicates that jet flows are roughly self-similar over several orders of magnitude in distance from the black hole. This is easiest to understand if the jets are mainly fluid phenomena so that they are governed by the laws of gas dynamics and magnetohydrodynamics.

Images of jets contain a bright, nearly unresolved “core” at the upstream end. This roughly stationary feature can represent a physical structure, such as a standing shock wave, or simply the most compact bright emission that is visible at the frequency of observation. In the latter case, the core can be at a different position at different wavelengths. The remainder of the jet tends to be knotty, although regions of smoothly varying intensity are sometimes present. On parsec scales imaged by very long baseline interferometry (VLBI), we find that many of the knots move, while other emission features appear stationary. Motions probably occur on kiloparsec scales as well, but monitoring over very long times is needed to detect such motions.

### 2.2 Motions inside Jets and Relativistic Beaming of Radiation

Strong evidence that some jets have relativistic flow velocities comes from sequences of VLBI images that show apparent superluminal motions of bright knots away from the core, as illustrated in Fig. 3. The apparent motion is faster than the actual speed  $\beta c$  because the emitting plasma approaches us at nearly the speed of light  $c$ . Therefore, it moves almost as fast as the radio waves it emits, so that the arrival times at Earth are compressed relative to those in the rest frame of the plasma. The apparent velocity in the plane of the sky is given by

$$v_{\text{app}} = \frac{\beta c \sin \theta}{1 - \beta \cos \theta}, \quad (1)$$

where  $\theta$  is the angle between the velocity vector and the line of sight. The apparent velocity is a maximum at  $\theta = \sin^{-1}(1/\Gamma)$ , where  $\Gamma = (1 - \beta^2)^{-1/2}$  is the Lorentz factor of the centroid of the “blob” of emitting plasma.

While the time scales involved make superluminal motion easiest to detect on parsec scales, a superluminal feature has been seen at least 120 parsecs from the nucleus in the relatively nearby radio galaxy M 87 [19].

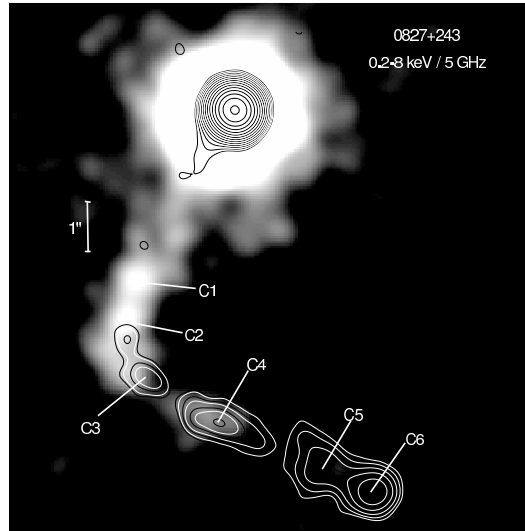


**Fig. 2.** Image of the jet of the quasar 0827+243 (OJ 248) at radio frequency 5 GHz (contours) and at X-ray photon energies (greyscale). The nucleus is the bright region near the top. At the redshift (0.939) of this quasar,  $1'' = 7.2$  kpc on the sky, but  $\sim 100$  kpc when de-projected. From [41]

The relativistic motion produces a strong Doppler effect that increases the observed frequency and decreases the time scales of variability by a factor

$$\delta = [\Gamma(1 - \beta \cos \theta)]^{-1}, \quad (2)$$

which is termed the “Doppler factor.” It is a maximum of  $(1 + \beta)\Gamma$  when  $\theta = 0$  and equals  $\Gamma$  when  $\theta = \sin^{-1}(1/\Gamma)$ . Because of relativistic aberration, most of the emission is beamed into a cone with an opening half-angle  $\sim \Gamma^{-1}$ , so that the flux density  $F_\nu$  of the plasma is boosted by a factor of  $\delta^2$ . Since the frequency  $\nu$  is also increased, if  $F_\nu \propto \nu^{-\alpha}$ , the flux density is a factor of  $\delta^{2+\alpha}$  higher than it would be if the velocity were much less than the speed of light. This applies if the emission comes from a feature in a steady state—a standing shock wave, for example. However, if the emitting plasma moves, as does a superluminal knot, there is another factor of  $\delta$  from the time compression ( $\Delta T \propto \nu^{-1} \propto \delta^{-1}$ ). We then have

$$F_\nu \propto \delta^{2+\alpha} \nu^{-\alpha} \quad (\text{steady state}) \quad (3)$$

$$F_\nu \propto \delta^{3+\alpha} \nu^{-\alpha} \quad (\text{moving plasma}). \quad (4)$$

Jets have basically conical shapes, with opening half-angles  $\phi$  ranging from  $\sim 5^\circ$  to considerably less than  $1^\circ$ . A study of jets in 15 AGN indicates that  $\phi \propto \Gamma^{-1}$  [42]. This implies that acceleration of jets to the highest velocities is related to their collimation toward a nearly cylindrical geometry.

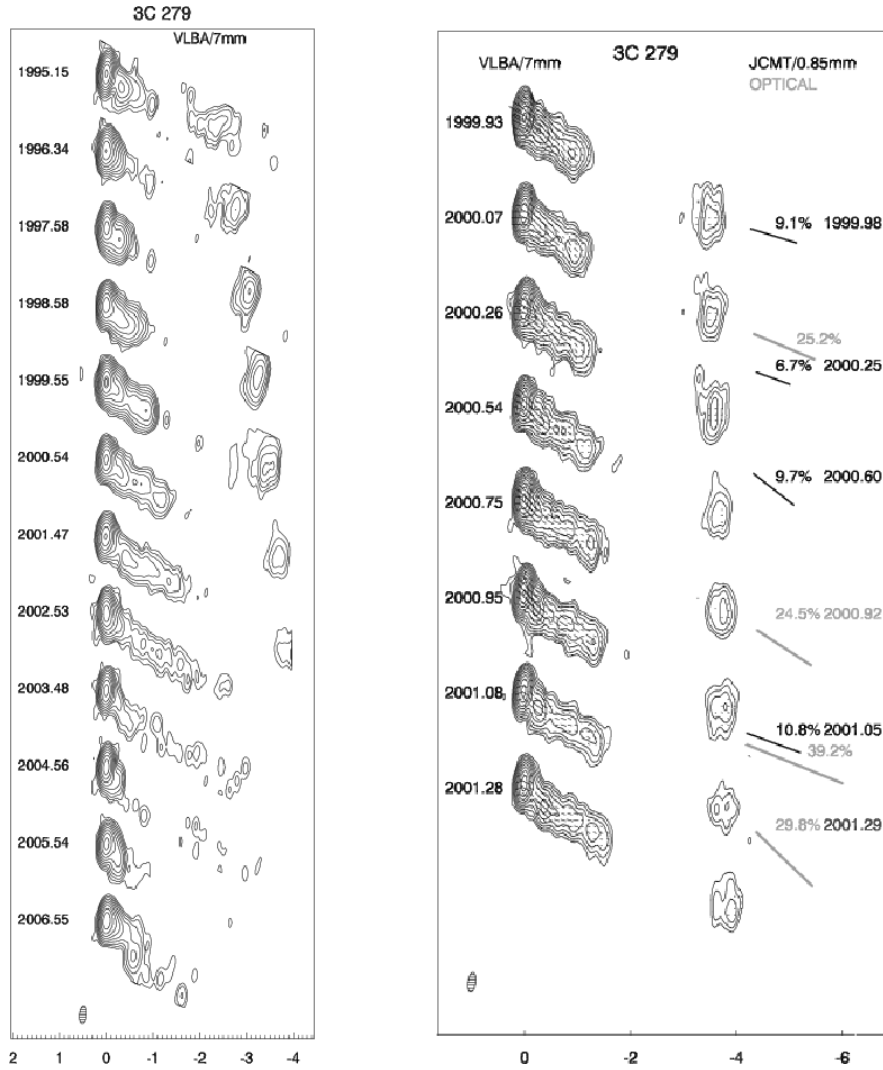


**Fig. 3. (Left)** Twelve-year sequence of annual VLBI images of the quasar 3C 279 at 43 GHz. At the redshift of the quasar, 1 mas = 6.3 pc. The feature at the narrow end of the jet, closest to the supermassive black hole, is referred to as the “core” and is assumed to be stationary. The motion of the outlying knot has an apparent superluminal speed of  $\sim 10c$ . Note the change in direction of the innermost jet with time. **(Right)** Sequence of roughly bimonthly images of 3C 279 showing the systematic growth of the length of the inner jet at a speed of  $13c$ . The linear polarization at 43 GHz is indicated by the sticks inside the contours, while the 230–350 GHz and optical polarization are given on the right-hand side of the figure. Images from author and S. Jorstad

### 2.3 Polarization

Jets are usually linearly polarized at a level that can be as high as 50% or greater for the more extended features, but more typically a few percent in the core. On the other hand, the circular polarization, with few exceptions, is generally less than 1%. This is the signature of incoherent synchrotron radiation, with relativistic electrons over a wide range of pitch angles spiraling in a magnetic field. The field can be nearly uniform over the resolution beam of the interferometer in the case of linear polarization of tens of percent. Lower levels of polarization indicate a chaotic magnetic field, which can be described roughly in terms of  $N$  cells of equal size, each with uniform but randomly oriented field. The degree of polarization is then

$$p = p_{\max} N^{-1/2} \pm p_{\max} (2N)^{-1/2}, \quad (5)$$

where  $p_{\max} = (\alpha + 1)/(\alpha + 5/3)$  is usually in the range of 0.7-0.75 [15].

The electric vector position angle (EVPA, or  $\chi$ ) of linear polarization is perpendicular to the projected direction of the magnetic field if the emission is from optically thin synchrotron radiation. However, relativistic motion aberrates the angles, an effect that causes the observed value of  $\chi$  to align more closely with the jet direction than is the case in the plasma rest frame. Because of this, polarization electric vectors observed to be roughly perpendicular to the jet axis correspond to magnetic fields that lie essentially parallel to the flow direction, but EVPAs that are modestly misaligned with the jet actually imply that the rest-frame magnetic field is quite oblique to the jet axis.

Faraday rotation alters the EVPA as well. If the synchrotron emission from the jet passes through a Faraday “screen”—e.g., a sheath of thermal plasma surrounding the jet—then the EVPA rotates by an amount

$$\Delta\chi = 7.27 \times 10^4 [\nu_{\text{GHz}}/(1+z)]^{-2} \int n_e B_{\parallel} ds_{\text{pc}} \text{ radians}, \quad (6)$$

where  $z$  is the redshift of the AGN,  $n_e$  is the electron density of the screen in  $\text{cm}^{-3}$ ,  $B_{\parallel}$  is the component of the screen’s magnetic field along the line of sight in gauss, and  $s_{\text{pc}}$  is the path length through the screen in parsecs. Any electron-proton plasma inside the jet also causes rotation, although the magnitude of  $\Delta\chi$  is reduced by the inverse of the average electron Lorentz factor  $\langle\gamma\rangle$ , where  $\gamma \equiv E/(m_e c^2)$ . Furthermore, when the rotation is distributed through the emission region,  $\Delta\chi$  is different for the different path lengths to the emission sites along the line of sight. Because of this, the net effect is partial depolarization of the radiation through cancellation of mutually orthogonal components of the rotated polarization vectors from the different sites.

The linear polarization of any part of the source that is optically thick to synchrotron self-absorption is reduced by a factor  $\sim 7$  from the maximum value—to  $\sim 10\%$  in the uniform field case. Further reductions caused by a lower degree of order of the magnetic field render self-absorbed synchrotron emission nearly unpolarized in most cases. The EVPA is transverse to that of optically thin emission, and is therefore parallel to the direction of the mean magnetic field.

Incoherent synchrotron radiation is circularly polarized at a level  $p_c \sim \gamma^{-1}(\nu)$ , where  $\gamma(\nu)$  is the Lorentz factor of the electrons whose critical frequency is the frequency of observation  $\nu$ :  $\gamma(\nu) = 6.0 \times 10^{-4} [\nu/(B\delta)]^{1/2}$ , where  $B$  is the magnetic field strength. This is generally much less than 1%. The circular polarization observed in

the compact jets, on the other hand, can be as high as 1-3% [82]. The likely cause is Faraday conversion of linear to circular polarization by electrons (and positrons, if present) with  $\gamma \sim 1 - 10$  [39].

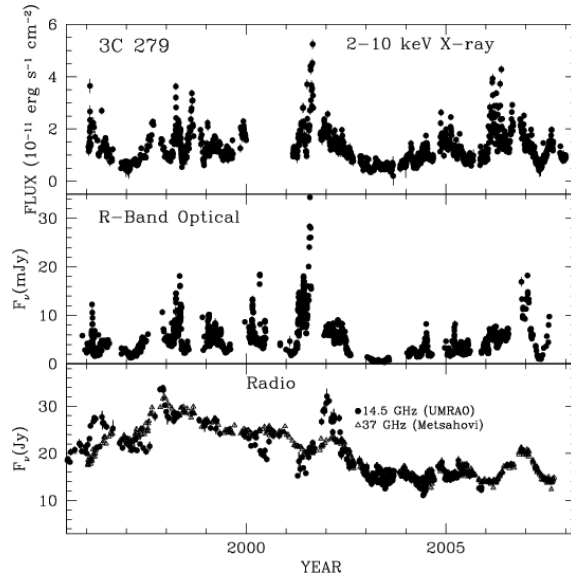


**Fig. 4.** Variation of flux vs. time of the quasar 3C 279 at X-ray, optical, and radio frequencies. From data of author and collaborators

### 2.4 Spectral Energy Distribution

A striking property of jets is their ability to radiate profusely from radio to  $\gamma$ -ray frequencies. As Figs. 1 and 2 illustrate, jets can be prominent in optical and X-ray images even at distances of hundreds of kiloparsecs from the nucleus. As seen in the quasar 3C 279 (Figs. 3 & 4 and [31]), the compact, parsec-scale jets of prominent blazars imaged by VLBI are the sites of bright radio through  $\gamma$ -ray emission that varies—often quite dramatically—on time scales as short as hours or even minutes. In some BL Lac objects, the fluctuating emission extends up to TeV  $\gamma$ -ray energies. The variations are often correlated across wavebands, sometimes with time delays.

Figure 5 displays the full electromagnetic continuum spectrum of 3C 279, with the main physical components of the emission identified. Synchrotron emission from the extended jet dominates at the lowest radio frequencies, while synchrotron radiation from the compact jet supplies most of the flux from GHz to optical frequencies. Thermal blackbody radiation from the accretion disk is prominent at ultraviolet frequencies, while inverse Compton scattering by relativistic electrons in the compact jet produces most of the X-rays at  $> 1$  keV and  $\gamma$  rays at  $< 100$  GeV energies in this quasar.

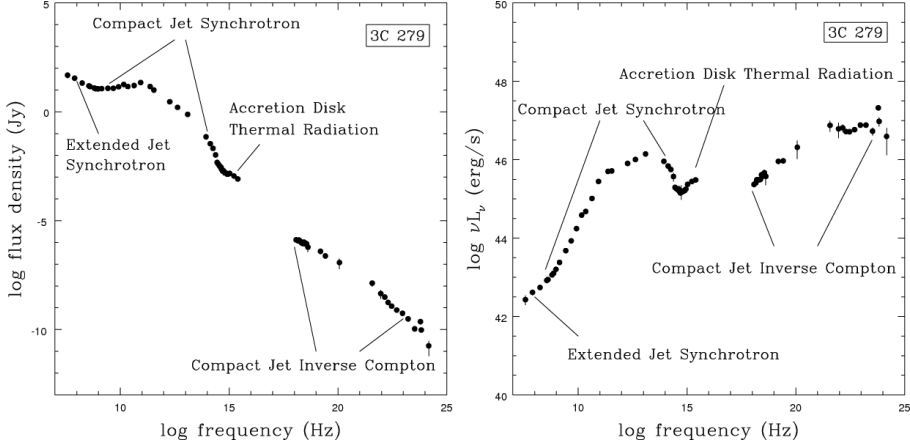


**Fig. 5. (Left)** Continuum spectrum of the quasar 3C 279. **(Right)** Same plot but with spectral luminosity along the vertical axis. The main emission components are indicated. From data compiled by the NASA Extragalactic Database plus data of the author and collaborators

The plot in the right panel of Fig. 5 emphasizes the spectral bands containing most of the *apparent* luminosity. Translation to *actual* luminosity, however, requires that we remove the effects of relativistic beaming by dividing by  $\delta^{2+\alpha}$  if the flux is steady and by  $\delta^{3+\alpha}$  if the spectrum corresponds to a temporary outburst. Since the Doppler factor of 3C 279 is  $\delta = 24 \pm 6$  [42], this requires division of the apparent luminosity of the jet by a factor exceeding 1000. In fact, the accretion disk is the most intrinsically luminous component in most quasars. This does not, however, imply that the *kinetic power* of jets is a negligible fraction of the overall luminosity, since jets are rather radiatively inefficient.

We can calculate the optically thin synchrotron flux density in the power-law portion of the spectrum of the steady-state jet by adopting a conical geometry with a magnetic field whose strength decreases with cross-sectional radius  $R$ ,  $B = B_0(R/R_0)^{-b}$ , and with a power-law electron density per unit energy,  $N(E) = N_0(R/R_0)^{-a}E^{-(1+2\alpha)}$ . Here  $R_0$  is the radius at the location where the emission turns on, presumably the point farthest upstream where electrons are accelerated to energies high enough to radiate at the rest frequency  $\nu(1+z)/\delta$ . Because of the gradients, we need to integrate the emission coefficient [67] over volume, divide by  $4\pi$  times the square of the luminosity distance  $D_l$ , and apply appropriate relativistic corrections:

$$F_\nu \approx (4\pi D_l^2)^{-1} c_1(\alpha) N_0 B_0^{1+\alpha} \delta^{2+\alpha} (1+z)^{1-\alpha} \nu^{-\alpha} \phi^2 \int_{Z_0}^{\infty} Z^{2-a-(\alpha+1)b} dZ, \quad (7)$$

where, in cgs units,  $c_1(\alpha) = 1.01 \times 10^{-18}$ ,  $3.54 \times 10^{-14}$ ,  $1.44 \times 10^{-9}$ ,  $6.30 \times 10^{-5}$ , and  $1.5 \times 10^5$  for  $\alpha = 0.25, 0.5, 0.75, 1.0$ , and  $1.5$ , respectively, incorporates numerical and physical constants (see [41, 58] for a tabulation),  $z$  is the redshift of the host galaxy,  $\phi$  is the opening half-angle of the jet in radians,  $Z$  is distance in pc from the black hole along the jet axis, and  $Z_0 = R_0/\sin \phi$ . The upper limit to the integral

is actually  $Z_{\max}(\nu)$ , the point where there are no longer substantial numbers of electrons that can radiate at rest frequency  $\nu(1+z)/\delta$ . However, if  $a > 2$  and  $b > 1$ , we can use infinity in practice as long as  $Z_{\max}(\nu) \gg Z_0$ . Equation (7) is valid under the approximation that the Doppler factor is essentially the same across the jet, which requires that  $\Gamma$  does not depend on  $R$  and that either the viewing angle  $\theta \gg \phi$  or  $\phi \ll \Gamma^{-1}$ . A more accurate calculation requires numerical integration over polar and azimuthal angles inside the jet.

Note the flatness of the radio spectrum in the left panel of Fig. 5, a property caused by opacity plus gradients in magnetic field strength and density of relativistic electrons. We can derive the shape of the spectrum by considering the ideal case of a jet pointing directly at us with an opening angle  $\phi \ll \Gamma^{-1}$  and a Doppler factor that does not vary significantly with  $R$ . We further approximate that emission with optical depth  $\tau > 1$  is completely opaque, while that at lower optical depths is completely transparent. This means that all the emission comes from radial distances  $Z > Z_m$ , where  $Z_m$  corresponds to the position in the jet where the optical depth along the line of sight is unity. In order to derive this quantity, we again need to integrate:

$$\tau \sim 1 \approx c_2(\alpha) N_0 B_0^{0.5(2\alpha+3)} \left[ \frac{\delta}{\nu(1+z)} \right]^{0.5(2\alpha+5)} \int_{Z_m}^{\infty} Z^{-a-0.5(2\alpha+3)b} dZ, \quad (8)$$

where  $c_2(\alpha)$  is  $2.29 \times 10^{12}$ ,  $1.17 \times 10^{17}$ ,  $6.42 \times 10^{21}$ , and  $3.5 \times 10^{26}$ , for  $\alpha = 0.25$ ,  $0.5$ ,  $0.75$ , and  $1.0$ , respectively. We can solve for  $Z_m$  after evaluating the integral:

$$Z_m \approx \left( c_2(\alpha) [a + 0.5(2\alpha + 3)b - 1]^{-1} N_0 B_0^{0.5(2\alpha+3)} \times \left[ \frac{\delta}{\nu(1+z)} \right]^{0.5(2\alpha+5)} \right)^{1/[a+0.5(2\alpha+3)b-1]}. \quad (9)$$

We can now calculate the approximate flux at frequency  $\nu < \nu_m$ , where  $\nu_m$  is the frequency at which the source is transparent down to  $Z_0$ , by replacing  $Z_0$  by  $Z_m$  in the lower limit of the integral in (7). (We can derive an expression for  $\nu_m$  by replacing  $Z_m$  with  $Z_0$  in (9) and solving for  $\nu$ .) Since the main result we want is the dependence on frequency, we express the answer as a proportionality:

$$F_\nu(\nu < \nu_m) \propto \nu^\zeta, \quad (10)$$

where

$$\zeta = \frac{4\alpha(b-1) + 5(a+b-3)}{2(a-1) + (2\alpha+3)}. \quad (11)$$

A completely flat spectrum, with  $\zeta = 0$ , is possible if  $a = 2$  and  $b = 1$ , as proposed by Königl [46]. While this value for  $b$  corresponds to the expected dependence of a transverse magnetic field on  $R$ , the value  $a = 2$  would only hold if adiabatic expansion cooling did not occur. If, on the other hand, expansion cooling is the main energy loss mechanism for the electrons, we expect  $a = (4/3)\alpha + 2$  in the case of a jet with constant flow Lorentz factor  $\Gamma$ . Since actual jets usually contain a number of knots in addition to the core, the flat spectrum must be caused by a superposition of the individual spectra of the various features, each peaking at different frequencies. The fact that these tend to produce composite spectra that are, to a rough approximation, flat, implies that Königl's ansatz is globally correct, even if it might not apply locally. For example, standing and/or moving shock waves in the jet can convert flow energy into plasma energy, whereas adiabatic expansion

cooling does the reverse. As long as only an insignificant fraction of the total flow energy is lost to radiation, the overall spectrum will follow the  $a = 2$ ,  $b = 1$  case. In fact, careful analysis of the jet in 3C 120 over several orders of magnitude in length scale indicates that it maintains the values  $a = 2$  and  $b = 1$  [81].

### 3 Physical Processes in AGN Jets

Considerable progress has been made in the interpretation of observations of jets by assuming that the main physical processes governing jets are those of gas dynamics and magneto-hydrodynamics (MHD). Plasma physics in the relativistic regime must also play a role in the heating and motions of the particles that compose jets. Unfortunately, our understanding of the relevant plasma phenomena is hindered by insufficient observations coupled with the likely complexity involved when the mean particle energy is relativistic. In addition, electrodynamics might govern the dynamics close to the black hole, and electrical currents can play an important role there and farther downstream. Here we will discuss some of the physical processes that have been successfully applied to explain a wide range of observations of jets.

#### 3.1 Launching of Jets

The basic requirement for producing a supersonic, highly collimated flow is a confinement mechanism coupled with a strong negative outward pressure gradient. In principle, this is possible with gas dynamics if the pressure of the interstellar medium in the nucleus drops by many orders of magnitude from the central regions to the point where the jet reaches its asymptotic Lorentz factor [11]. However, the most extreme jets are accelerated to  $\Gamma > 10$  and collimated to  $\phi < 1^\circ$  within  $\sim 1$  pc from the central engine [42]. At this location, the pressure in the jet is typically of order  $0.1 \text{ dyne cm}^{-2}$  (e.g., [63]). Gas dynamical acceleration and collimation would then require an external pressure  $\sim 10^4 \text{ dyne cm}^{-2}$  within  $\sim 0.01$  pc of the black hole. If this were provided, for example, by a hot ( $\sim 10^8$  K) wind emanating from the accretion disk, the X-ray luminosity would be enormous,  $\sim 10^{50} \text{ erg s}^{-1}$ .

For this reason, magnetic launching is considered to be the driving force behind most relativistic jets in AGN. The differential rotation of the ergosphere of a spinning black hole and/or accretion disk causes the component of the magnetic field lines of the accreting matter to wind up into a helix. The toroidal component of the wound-up field,  $B_{\text{tor}}$ , provides a pinching force through the hoop stress, with magnitude  $F_{\text{pinch}} = B_{\text{tor}}^2 / (4\pi R)$ , directed toward the jet axis. The magnetic field expands with distance from the black hole, lowering the magnetic pressure. This creates a strong pressure gradient along the axis, which accelerates the flow. In order for the velocity to become highly relativistic, the magnetic energy density must greatly exceed the rest-mass energy density at the base of the jet. Hence, the flow is initially dominated by Poynting flux that is transferred to kinetic flux of the particles in the jet toward greater axial distances  $Z$ .

The magnetic acceleration essentially stops when the kinetic energy density of the particles reaches equipartition with the magnetic energy density. Therefore, the final flow Lorentz factor is [80]

$$\Gamma_{\text{max}}(Z) \sim (B_i^2) / [16\pi n(Z) \langle m \rangle c^2], \quad (12)$$

where  $n(Z)\langle m \rangle$  is the mass density of particles at position  $Z$ , and  $B_i$  is the magnetic field at the base of the jet.

In the magnetic (as well as gas dynamical) acceleration model, the opening angle  $\phi$  is inversely proportional to the final Lorentz factor, as observed [42]. The gradual acceleration implies that any radiation from the innermost jet is weakly beamed relative to that on parsec scales. Therefore, one should expect that most of the observed emission arises from regions near and downstream of the core seen on millimeter-wave VLBI images, even at high frequencies where the entire jet is transparent.

### 3.2 Gas Dynamics of Jets

Since jets are long-lived phenomena, we can assume that, to first order, they represent steady flows. Then the relativistic Bernoulli equation applies:

$$\Gamma(u + p)/n = \text{constant}, \quad (13)$$

where  $u$  is the energy density of the plasma,  $p$  is the pressure, and  $n$  is the number density of particles, all measured in the co-moving reference frame. If the mean energy per particle  $\langle E \rangle$  greatly exceeds the mean rest-mass energy, then  $u = 3p = n\langle \gamma m \rangle c^2$ . In addition, the ideal gas law for a relativistic plasma can be expressed as  $p \propto n^{4/3}$ . We can use these expressions in (13) to obtain

$$\Gamma(Z) = \Gamma(Z_0)[p(Z_0)/p(Z)]^{1/4}, \quad (14)$$

where  $Z_0$  is a reference point. This is the relativistic version of Bernoulli's principle, which states that the velocity of a flow is inversely related to its pressure.

We could also rearrange the ideal gas law to write  $\langle \gamma \rangle \propto n^{1/3}$  and

$$\Gamma(Z) = \Gamma(Z_0)\langle \gamma(Z_0) \rangle / \langle \gamma(Z) \rangle. \quad (15)$$

This formulation emphasizes that the acceleration of the flow results from conversion of internal energy into bulk kinetic energy. Significant increase in the flow speed through gas dynamics is no longer possible if  $\langle \gamma(Z) \rangle$  is not substantially greater than unity. Beyond this point, the jet will be ballistic, coasting at a constant velocity until it is disturbed.

The cross-sectional area of a jet will tend to expand and contract such that the pressure at the boundary matches the external pressure. The maximum opening angle  $\phi$ , however, is the inverse of the Mach number at the point where the pressure drop occurs,  $\phi_{\max} = v_s/(\Gamma\beta c)$ , where  $v_s$  is the local sound speed.

Since the interstellar medium is dynamic, and since the pressure in the jet is subject to time variability, a jet is likely to be subject to mismatches in pressure at the boundary. If modest in magnitude, the difference in pressure is accommodated through sound waves that communicate the pressure imbalance to the jet interior. This causes both oscillations in the cross-sectional radius as well as compressions and rarefactions inside the jet [21]. The Lorentz factor is higher in the lower pressure regions and lower where the pressure is greater. If the pressure mismatch exceeds  $\sim 50\%$ , oblique "recollimation" shock waves form to adjust the flow more abruptly. If the jet is sufficiently circularly symmetric, the shock waves will be conical. If the symmetry is nearly perfect, the conical shock is truncated by a strong shock aligned

perpendicular to the axis, called a “Mach disk.” Since the role of a shock front is to decelerate a disturbed supersonic flow to subsonic velocities, the flow will cease to be highly relativistic until it reaccelerates where it encounters a pronounced rarefaction downstream of the Mach disk. Shock waves set up by pressure mismatches with the surrounding medium are often labeled “external” since they are driven by influences from outside the jet.

“Internal” shock waves can result from changes in the jet velocity or injected energy at or near the base. A major disturbance is required to generate a shock when the flow velocity is near the speed of light, since the relative velocity needs to be supersonic. If the local sound speed is the fully relativistic value,  $c/\sqrt{3}$ , then the Lorentz factor of the faster flow must be at least a factor  $\sim 2$  higher than that of the slower flow that it overtakes.

A shock compresses the plasma so that the density rises by a factor  $\xi$  across the shock front. The magnetic field component that lies parallel to the shock front increases by the same factor, while the component transverse to this direction remains unchanged. The maximum value of  $\xi$  is 4 in a thermal plasma; it can be higher in relativistic plasma, but if the jet flow is already highly relativistic, disturbances are unlikely to be sufficiently strong relative to the quiescent flow for values of  $\xi$  greater than about 2 to be common. In the reference frame of the shock front, the undisturbed plasma flows in at a supersonic velocity and exits at a subsonic speed. Unless the sound speed is close to  $c$ —the maximum value of  $c/\sqrt{3}$  requires that the plasma be highly relativistic, with  $\langle\gamma\rangle \gg 1$ —this means that the shocked plasma will have a bulk Lorentz factor only slightly lower than that of the shock front.

### 3.3 Magnetohydrodynamics of AGN Jets

The gas dynamical description of a jet is valid as long as the energy density of the magnetic field is significantly less than that of the particles. In this case, the field is “frozen in” and will follow the plasma. Close to the black hole, however, the magnetic field plays a major role in the dynamics, and even on kiloparsec scales the field energy is probably roughly in equipartition with that of the particles.

Section 3.1 above briefly summarizes the MHD forces that can accelerate and collimate a jet in the inner parsec. This depends on a strong toroidal component of the magnetic field, which itself requires a radial electric current. Since the system has considerable angular momentum, the streamlines that the flow follows trace out a spiral pattern about the axis [79].

When the magnetic field is mainly toroidal, kinks that occur in the jet are subject to a current-driven instability that causes the kinks to grow [5]. Simulations indicate that the net result is to convert Poynting flux into internal energy of the plasma [29].

We therefore have a crude theoretical description of a jet that is collimated by a toroidal magnetic field and accelerated by a decreasing magnetic pressure gradient, but eventually subject to an internal instability that heats the plasma. By the time such a jet reaches parsec scales, it has a relativistic flow velocity, contains a magnetic field that is at least somewhat chaotic, and is loaded with relativistic electrons (and either protons or positrons, or both). These are the necessary ingredients to produce the jets observed on VLBI images, with bright synchrotron and inverse Compton emission and fairly weak linear polarization.

### 3.4 Instabilities in Jets

As the parsec to kiloparsec-scale continuity of jets like the one in 3C 273 displayed in Fig. 1 demonstrates, many jets are stable over extremely large distances. Jets that are completely free, i.e., containing higher pressure than their surroundings and propagating ballistically, are inherently stable. However, if their cross-sections are able to adjust to maintain pressure equilibrium with the external medium, they are subject to the Kelvin-Helmholtz instability that occurs when two fluids have different velocities adjacent to a tangential discontinuity. These instabilities have numerous modes that are divided into two classes, body modes and surface modes. The body modes cause departure of the cross-sectional geometry from circular symmetry as well as oscillations of the transverse radius and filamentary structure [29]. Figure 6 shows an example of such a jet. The surface modes generate turbulence and velocity shear at the boundaries that can permeate the entire jet cross-section as the instability grows.

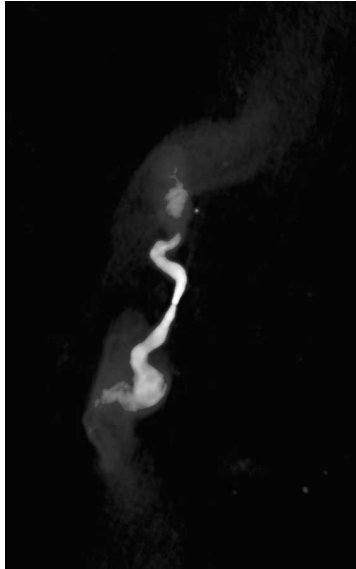


**Fig. 6.** Radio image of the FR I radio galaxy 3C 31 showing a two-side jet that becomes globally unstable. The nucleus is in the middle of the straight section of the jet. Image courtesy of NRAO/AUI/NSF, data published in [50]

The reason why jets can remain largely intact hundreds of kiloparsecs from their site of origin in the nucleus is that Kelvin-Helmoltz instabilities are suppressed at higher Mach numbers and Lorentz factors, and when there is a strong axial magnetic field. These characteristics are found in the most powerful jets, those of the FR II quasars and radio galaxies.

Since they can lead to the development of turbulence and formation of shocks, instabilities might be the cause of much of the emission seen on parsec and kiloparsec scales [74]. In addition, much of the rich structure seen in some jets might owe its

existence to such instabilities. The turbulence in the boundary region also promotes entrainment of material from the surrounding medium [8, 49], a process that slows the jet down [52], eventually leading to its disruption in FR I sources.

### 3.5 Cross-Jet Structure

Jets can possess structure transverse to the axis whether or not instabilities develop. In fact, theoretical models and simulations of jet launching generally predict such structure [76, 69, 65, 80, 32, 64]. Although there can be a smooth gradient in density and velocity [80], transverse structure is often described as an ultra-fast spine surrounded by a more slowly moving sheath. The spine is predicted by many theories to be composed of an electron-positron pair plasma, with the sheath containing a normal electron-proton mixture [76, 69, 64]. While there is considerable observational evidence for cross-jet structure [52, 70, 42], it is not yet clear whether there is a smooth gradient in properties or a two-layer structure.

### 3.6 Magnetic Field

As discussed previously, we expect the magnetic field to have a tight helical geometry close to the black hole. At the end of this acceleration and collimation zone, current-driven instabilities mix the field into a more chaotic configuration. Velocity shear can either align the magnetic field parallel to the axis or generate turbulence that disorders the field. In the former case, one can imagine closed loops of field lines that are stretched by the relative velocity between faster flow closer to the axis and slower layers closer to the boundary.

As in any spherical or conical flow in which magnetic flux is conserved, the axial component of the magnetic field decreases as  $R^{-2}$ . The component transverse to the axis should decrease as  $R^{-1}$ . There are numerous examples of extended jets in which the expected transition from longitudinal to transverse magnetic field is evident in the linear polarization [13]. However, comparison of simulated and observed polarization indicates that, while the toroidal to longitudinal magnetic field ratio does increase with distance down the jet, the gradient in the ratio is not as steep as predicted in the case of a magnetic field that is frozen into the plasma [51]. There is instead a substantial component of disordered field that has a more complex behavior.

### 3.7 Energization of Electrons

Since the radiation from AGN jets comes from electrons (and positrons, if any), the sites of strong emission are strongly related to the processes that accelerate electrons to Lorentz factors  $\gamma$  that can exceed  $10^6$  on both subparsec and kiloparsec scales in some jets. The power-law shape with slope  $-\alpha$  of the optically thin synchrotron spectrum over  $\sim 4$  orders of magnitude (see Fig. 5) implies that the electron energy distribution is also a power law, with slope (on a log-log plot)  $-(2\alpha + 1)$  over at least 2 orders of magnitude in  $\gamma$ .

A long-standing explanation for a power-law electron energy distribution is the Fermi mechanism [25]. Particles repeatedly reflect off regions of higher-than-average magnetic fields, gaining energy if the region was moving toward the particle (in

the plasma’s rest frame) and losing energy if it was receding. The net result is a power-law energy distribution. If a particle gains an average energy  $\Delta E = \xi E$  per reflection and if the probability of staying in the acceleration zone after a reflection is  $\eta$ ,  $\alpha = \ln \xi / (2 \ln \eta)$ . The process can produce very high energies if  $\eta$  is close to unity so that a typical particle encounters many reflections before exiting the zone.

One site where the Fermi mechanism can be particularly efficient is at a shock front. In this case,  $\xi = (4\Delta u)/(3c)$ , where  $\Delta u$  is the increase in flow velocity across the shock front [7]. Plasma waves are likely to be present on both sides of the shock. These reflect the particles so that they pass back and forth across the shock multiple times. Less systematic acceleration of particles can occur in a turbulent region since, statistically, the number of approaching collisions with cells of higher than average magnetic field is greater than the number of receding collisions. The mean fractional energy gain per reflection is  $\xi \approx 4(\Gamma_{cell} v_{cell}/c)^2$ . Therefore, the process is efficient if the turbulence is relativistic, as one might expect if the jet has substantial transverse velocity gradients.

An unresolved issue with the Fermi mechanism is how it can produce a similar power-law slope in remotely separate physical regions. For example, the spectral index in the jet of 3C 120  $\alpha \approx 0.65$  over several orders of magnitude in size scale [81]. If the bright emission regions are caused by shocks, all the shocks would need to have the same compression ratio, which would seem difficult to engineer. If turbulent processes energize the particles, the physical conditions would again need to be more similar than one might expect over such a large range of size scales.

## 4 Physical Description of Features Observed in Jets

### 4.1 The Core

The core is generally the most compact part of a jet that we can image at any given frequency. This implies that an understanding of its nature can provide insights into the physical structure of jets at and perhaps upstream of the core’s position. As we have discussed above, what is seen as the core on VLBI images at radio frequencies might be the transition region between optically thick and thin emission. However, it could also be a bright, stationary emission structure a short distance downstream of that region. If the core is the surface where the optical depth is near unity, its position  $Z_m$  should move toward  $Z_0$  and therefore toward the central engine at higher frequencies. This effect is apparent in some compact extragalactic jets [54], but not in others [66]. The implication of the latter negative result is that the jet is not just a smooth flow punctuated by superluminal knots, but also contains multiple bright stationary features. In the quasar 0420–014, observations of fluctuating polarization in the core and at optical wavelengths have been interpreted as the signature of turbulent jet plasma passing through a standing conical shock system—perhaps an example of a recollimation shock discussed in Sect. 3.2—that represents the physical structure of the core [23].

In some objects the core could be a bend in the jet where it becomes more closely aligned with the line of sight. This would cause an increase in the Doppler beaming factor relative to points farther upstream. This cannot be the main reason for the appearance of cores, however, since it is less likely for a jet to curve toward than away from the line of sight.

While jets are often approximately self-similar on parsec scales, this must break down close to the central engine in the flow acceleration and collimation zone (ACZ). The point where the change must occur is indicated by the frequency above which the synchrotron spectrum steepens, signaling that the jet emission is optically thin. According to observations [38], this is in the range of tens to  $> 1000$  GHz. (It is  $10^{11}$  Hz in Fig. 5.) The angular width of the jet at this point can be estimated by the value at 43 GHz,  $\sim 50 \mu\text{arcsec}$  times  $43 \text{ GHz}/\nu_m$ . For a quasar with redshift of order 0.5, this translates to  $\sim 0.3(43 \text{ GHz}/\nu_m)$  pc, which is small (a few  $10^{16}$  cm for  $\nu_m \sim 1000$  GHz) but still hundreds of Schwarzschild radii even for a black hole mass  $\sim 10^9 M_\odot$ . The distance of the end of the ACZ from the black hole might be many times larger than this. The flux of radiation from a blazar jet inside the ACZ probably decreases toward the black hole, since the relativistic beaming is weaker owing to the progressively lower flow Lorentz factor [56]. In the jet of a radio galaxy viewed nearly side-on, however, the emission should become stronger (as long as there are energetic electrons) toward smaller distances from the black hole, since the radiation is anti-beamed. This implies that there should be a very short gap between the start of the jet and the beginning of the counterjet, except for a limited section obscured by free-free opacity in the accretion disk and dusty torus beyond the disk. Furthermore, the flow should start out fairly broad and become more collimated as it accelerates downstream. VLBA observations of the radio galaxy M87, whose relatively local distance allows a linear resolution of tens of gravitational radii, indicate that the flow is indeed quite broad near the central engine [43].

## 4.2 Quasi-stationary Features

Besides the core, there are often other bright features in blazar jets that are either stationary or move at subluminal apparent speeds [40, 45, 42]. In straight jets, these can be produced by recollimation shocks or instabilities (see Sect. 3.2 and Sect. 3.4) that compress the flow or excite turbulence. This should lead to particle acceleration and amplification of the magnetic field, and therefore enhanced emission.

Bends can also cause quasi-stationary hotspots, either because the jet turns more into the line of sight [1] or from the formation of a shock. An example of the latter is the collision of the jet with an interstellar cloud. In this case, an oblique shock forms to deflect the jet flow away from the cloud.

Long-lived jets propagate through their host galaxy and into the intergalactic medium. In the case of low-luminosity, FR I sources (e.g., the one shown in Fig. 6), instabilities at the boundary and entrainment of the external gas decelerate the jet to subsonic speeds and completely disrupt it. The more powerful FR II jets generally survive out to the point where a strong termination shock decelerates them to subsonic speeds. The shock appears as a bright, compact hotspot, while the jet plasma spreads into a giant turbulent “lobe” that emits radio synchrotron radiation (see Fig. 7). As inferred by the ratio of distances from the nucleus of the near and far lobes, the termination shock moves subluminally away from the galaxy as the momentum of the jet pushes away the external gas.

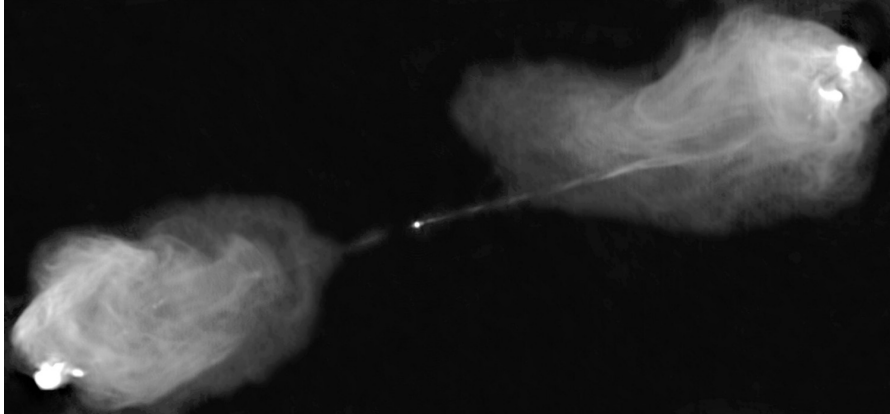


**Fig. 7.** Radio image of the FR II radio galaxy Cygnus A showing the small, bright core at the center, two-side jet, billowy lobes, and hotspots at the outer edges of the lobes. The western side approaches us, hence the lobe is farther from the core since the hotspots and lobes move outward with time and we see the eastern lobe at an earlier time owing to light-travel delay. Image courtesy of NRAO/AUI/NSF, published in [68]

### 4.3 Models for Superluminal Knots in Jets

The bright knots that appear to move superluminally down compact jets (see Fig. 3) must represent regions of higher relativistic electron density and/or magnetic field than the ambient jet. They could be coherent structures, such as propagating shock waves caused by surges in the energy density or velocity injected into the jet at its origin near the central engine. However, they could also be “blobs” of turbulent plasma with electrons accelerated by the second-order, statistical Fermi process, i.e., random encounters with magnetic irregularities moving in various directions. Or, they might be ribbons or filaments generated by instabilities that move down the jet. It is likely that each of these possibilities occurs in some jets.

Shock waves are the most common interpretation of superluminal knots, since basic shock models have enjoyed considerable success at reproducing time variations of continuum spectra and polarization [60, 36, 37]. At frequencies above  $\sim 10$  GHz, radiative energy losses of the electrons can be important. In this case, if we assume that electrons are accelerated only at the shock front, they will lose their ability to produce synchrotron radiation at high frequencies as they advect away from the front and lose energy, since they cannot radiate much above their critical frequency,  $\nu_{\text{crit}} = 2.8 \times 10^6 B \gamma^2$  (in cgs units). This results in frequency stratification, with the highest frequency emission confined to a thin layer behind the shock front and progressively lower frequency emission occupying larger volumes. Figure 8 illustrates the effect. We can derive a proportionality between distance  $x$  behind the front and the frequency of emission that is limited to a shell of thickness  $x$  if we assume that the magnetic field and advection speed  $v_{\text{ad}}$  are constant out to distance  $x$  from the shock front:

$$x(\nu) \propto \nu^{-1/2}. \quad (16)$$

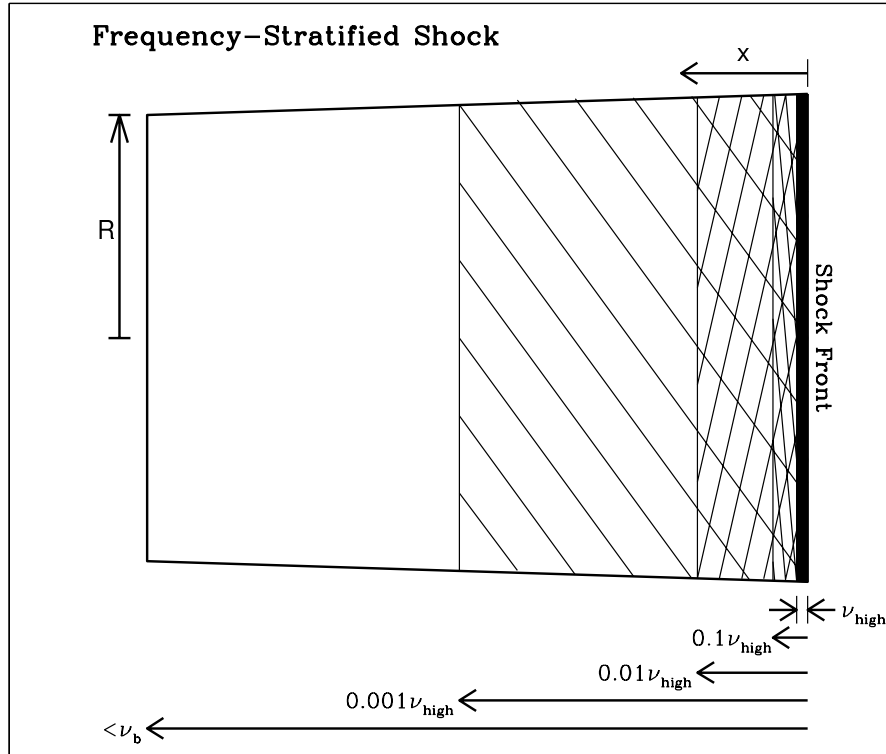


**Fig. 8.** Frequency stratification in a square-wave shock, drawn to scale. The electrons are accelerated at the shock front and drift behind the shock while losing energy to radiative losses. This example is for a forward propagating shock; the same principle is valid for a reverse or stationary shock, as well as for a shock that is oblique to the jet axis. See [60] for more details

Here, we have applied the solution to the synchrotron energy loss equation,  $\gamma_{\text{max}} \approx (1.3 \times 10^{-9} B^2 x / v_{\text{ad}})^{-1}$ . The volume of the emitting region is then  $\pi R^2 x \propto \nu^{-1/2}$ . This steepens the optically thin spectral index from  $\alpha$  to  $\alpha + 0.5$  at frequencies  $\nu \gg \nu_b$ , where  $\nu_b$  is the frequency at which  $x(\nu)$  equals the entire length of the shocked region, and  $-\alpha$  is the spectral slope of the emission coefficient. It also affects the time evolution of the flux density and turnover frequency as the shock expands while it propagates down the jet. In particular, at frequencies where synchrotron losses are greater than expansion cooling, the peak in the spectrum propagates toward lower frequencies while the flux density at the peak remains roughly constant [60]. This can contribute to the flatness of the overall synchrotron spectrum at radio frequencies.

The stratification results in time lags in the optically thin synchrotron radiation during the outburst caused by the formation of the shock, with higher frequency variations leading those at lower frequencies. Even beyond the point where the magnetic field is too low for synchrotron losses to compete with expansion cooling, time

delays at radio frequencies continue owing to the outburst becoming transparent at progressively lower frequencies with time. Lower amplitude flares and flickering (cf. the light curves displayed in Fig. 4) can be explained as the consequence of shocks compressing turbulent cells that they pass [61]. In this case, the higher frequency variations in flux density and polarization occur on shorter timescales because of the smaller volumes involved.

For the sake of simplicity, shocks in jets are usually modeled as transverse square waves in attempts to reproduce the observed variability of emission and polarization. Such shocks will compress the magnetic field component lying parallel to the shock front. In most jets showing superluminal motion, the orientation of the shock front is aberrated to appear nearly transverse to the jet axis in the observer's frame. This should yield linear polarization with electric vectors aligned along the jet axis. A large sample of quasar jets [53] observed with VLBI possess a distribution of polarization directions that is inconsistent with this assumption. Instead, the magnetic field seems to be mostly turbulent, with a small uniform component that is parallel to the jet axis. Other polarization observations [2] indicate that, if most superluminal knots are shocks, the fronts must be oblique to the jet axis in most cases.

The main differences between shock and blob models are the absence of frequency stratification in the latter and that it is unnecessary for the particles and magnetic field in a blob to be directly related to those of the surrounding jet plasma. In the case of an outburst of 3C 273, an attempt to model the event in terms of an expanding blob led to the nonsensical requirement that the magnetic field would need to have decreased while the particle density increased to reproduce the time behavior of the flare's continuum spectrum [60]. On the other hand, it is common to model X-ray synchrotron and  $\gamma$ -ray inverse Compton flares in BL Lac objects as blobs (e.g., [44]).

#### 4.4 Internal Energy and Kinetic Power

There are basically two methods for determining the energy contained in relativistic particles in extragalactic jets. The first is to assume equipartition between the magnetic and particle energy densities, which is similar to calculating the minimum energy required to produce the synchrotron emission [14]. We can express the ratio of relativistic particle to magnetic energy density as  $u_p/u_{\text{mag}} \equiv A$ , with  $A = 1$  corresponding to equipartition. If  $k$  is the fraction of particle energy that is contained in neither electrons nor positrons, the energy density in particles is

$$u_p = (1 + k)N_0 \int_{\gamma_{\text{min}} m_e c^2}^{\gamma_{\text{max}} m_e c^2} E^{-2\alpha} dE, \quad (17)$$

which we can set equal to  $Au_{\text{mag}} = AB^2/(8\pi)$ .

If we consider a section of volume  $V$  inside the jet, with radiation coming from some fraction  $f$  (the "filling factor") of that volume, and observe it to have a flux density  $F_\nu$  at a frequency  $\nu$  where the emission is optically thin, we can write

$$F_\nu \approx c_1(\alpha) D_l^{-2} f V N_0 B^{1+\alpha} \delta^{3+\alpha} (1+z)^{1-\alpha} \nu^{-\alpha}. \quad (18)$$

Here we have assumed that the measurement is for a moving knot; if it is a section of the steady-state jet, the exponent of  $\delta$  should be  $2 + \alpha$ . We can solve this equation

for  $N_0$ , substitute the result for  $N_0$  in (18), and set  $u_p$  equal to  $AB^2/(8\pi)$ . After evaluation of the integral, some algebraic manipulation, and conversion of various parameters into more readily observable quantities, we arrive at

$$B = c_4(\alpha)\delta^{-1}(1+z)^{(5+\alpha)/(3+\alpha)} \times \\ \times \left[ \frac{1+k}{Af} g(\alpha, \gamma_{\min}, \gamma_{\max}) D_{\text{Gpc}}^{-1} \Theta_{\text{as}}^{-3} F_{\text{mJy}} \nu_{\text{GHz}}^\alpha \right]^{1/(3+\alpha)} \mu\text{G}. \quad (19)$$

Here  $D_{\text{Gpc}}$  is the luminosity distance in Gpc,  $\Theta_{\text{as}}$  is the angular size in arcseconds (under the approximation of spherical symmetry),  $F_{\text{mJy}}$  is the flux density in milliJanskys ( $1 \text{ mJy} = 10^{-26} \text{ erg s}^{-1} \text{ cm}^{-2} \text{ Hz}^{-1}$ ),  $\nu_{\text{GHz}}$  is the observed frequency in GHz, and

$$g(\alpha, \gamma_{\min}, \gamma_{\max}) \equiv (2\alpha - 1)^{-1} [\gamma_{\min}^{-(2\alpha-1)} - \gamma_{\max}^{-(2\alpha-1)}] \quad (20)$$

except for the case  $\alpha = 0.5$  for which  $g = \ln(\gamma_{\max}/\gamma_{\min})$ . The function  $c_4(\alpha)$ , which is tabulated in [41], has a value of 1.9, 7.8, 25, 74, 170, and 380 for  $\alpha = 0.25, 0.5, 0.75, 1, 1.25,$  and  $1.5$ , respectively. The total energy density is  $(A+1)B^2/(8\pi)$ , hence the kinetic power is  $(\pi R^2 c) \Gamma^2 (A+1)B^2/(8\pi)$ .

For typical spectral indices in extended jets,  $\alpha = 0.8 \pm 0.2$ , it is mainly  $\gamma_{\min}$  that determines the value of the function  $g$ . Unfortunately, we cannot in general determine  $\gamma_{\min}$  accurately, since electrons at this energy radiate mainly in the MHz range or lower where the emission has many components that are difficult to disentangle. We also do not have reliable methods to estimate the parameters  $f$ ,  $A$ , or  $k$ . The usual procedure is to assume  $f = 1$ ,  $A = 1$  and  $k = 1$ , and some fairly high value of  $\gamma_{\min}$ , e.g., 100–1000, in order to derive a lower limit to the kinetic power. The powers thus calculated can be very high in quasar jets, exceeding  $10^{46} \text{ erg s}^{-1}$  in many cases, and as high as  $10^{48} \text{ erg s}^{-1}$  if  $\gamma_{\min} \sim 10$  or if the ratio of proton to electron energy density  $k$  is closer to 100, as is the case for cosmic rays in our Galaxy. The observational data are usually consistent with rough equipartition between the energy densities in electrons and in magnetic field under the assumption that  $k \sim 1$ .

The second method for deriving the energy content of jets is to analyze compact knots that are synchrotron self-absorbed, in which case there are two equations, one for the flux density and the other for the optical depth (which is close to unity at the frequency  $\nu_m$  of maximum flux density). We can then solve separately for  $B$  and  $N_0$  (see, e.g., [57]). The magnetic field can be expressed as

$$B = 3.6 \times 10^{-5} c_b(\alpha) \Theta_{\text{mas}}^4 \nu_{\text{m,GHz}}^5 F_{\text{mJy}}^{-2} \delta (1+z)^{-1} \\ = 0.011 c_b(\alpha) T_{\text{m,11}}^{-2} \nu_{\text{m,GHz}} \delta (1+z)^{-1}, \quad (21)$$

where the units are indicated by the subscripts and  $T_{\text{m,11}}$  is the brightness temperature at  $\nu_m$  in units of  $10^{11}$  K. The function  $c_b(\alpha)$  is 0.50, 0.89, 1.0, and 1.06 for  $\alpha = 0.25, 0.5, 0.75,$  and  $1.0$ , respectively. The similar equation for  $N_0$  is

$$N_0 = 0.012 c_n(\alpha) D_{\text{Gpc}}^{-1} \Theta_{\text{mas}}^{-(7+4\alpha)} \nu_{\text{m,GHz}}^{-(5+4\alpha)} F_{\text{mJy}}^{3+2\alpha} \delta^{-2(2+\alpha)} (1+z)^{2(3+\alpha)} \\ = 0.012 (17.7)^{-(3+2\alpha)} c_n(\alpha) D_{\text{Gpc}}^{-1} T_{\text{m,11}}^{3+2\alpha} \nu_{\text{m,GHz}} \Theta_{\text{mas}}^{-1} (1+z)^3 \delta^{-1}, \quad (22)$$

where  $c_n(\alpha)$  is 660, 22, 1.0, and 0.049 for  $\alpha = 0.25, 0.5, 0.75,$  and  $1.0$ , respectively.

We can therefore express the ratio of the relativistic electron to magnetic energy density mainly in terms of the brightness temperature:

$$u_{\text{re}}/u_{\text{mag}} \approx g_u(\alpha, \gamma_{\min}, \gamma_{\max}) T_{\text{m,11}}^{7+2\alpha} (D_{\text{Gpc}} \nu_{\text{m,GHz}} \Theta_{\text{mas}})^{-1} (1+z)^5 \delta^{-3}, \quad (23)$$

where

$$\begin{aligned}
 g_{\text{u}}(\alpha, \gamma_{\text{min}}, \gamma_{\text{max}}) &\approx 0.48\gamma_{\text{max}}^{0.5} & (\alpha = 0.25) \\
 &0.69\ln(\gamma_{\text{max}}/\gamma_{\text{min}}) & (\alpha = 0.5) \\
 &13\gamma_{\text{min}}^{-0.5} & (\alpha = 0.75) \\
 &74\gamma_{\text{min}}^{-1} & (\alpha = 1.0).
 \end{aligned} \tag{24}$$

We can invert (23) to determine an “equipartition brightness temperature,”

$$T_{\text{eq}} \approx 10^{11} [D_{\text{Gpc}} \nu_{\text{m, GHz}} \Theta_{\text{mas}} (1+z)^{-5} \delta^3 g_{\text{u}}^{-1}(\alpha, \gamma_{\text{min}}, \gamma_{\text{max}})]^{1/(7+2\alpha)} \text{ K}. \tag{25}$$

Features with brightness temperatures higher than this have energy densities dominated by relativistic particles.

Use of this method requires very accurate measurements of the angular size  $\Theta$ , spectral turnover frequency  $\nu_{\text{m}}$ , and flux density at the turnover  $F_{\text{m}}$  of individual features in jets, a difficult undertaking requiring multifrequency VLBI observations. With current VLBI, restricted to Earth-diameter baselines at high radio frequencies, only a relatively small number of well-observed knots have properties amenable to reliable estimates of the physical parameters. Application of this method to semi-compact jets (between parsec and kiloparsec scales, observed at frequencies less than 1 GHz), indicates that jets are close to equipartition on these scales [71]. The same may be true for the parsec-scale cores, although some cores and individual very compact knots can have particle energy densities greatly exceeding  $B^2/(8\pi)$  [33, 63].

#### 4.5 Inverse Compton X-ray and $\gamma$ -ray Emission

Derivation of the magnetic field and  $N_0$  allows the calculation of the flux of high-energy photons from inverse Compton scattering. If the “seed” photons that the relativistic electrons scatter are produced by synchrotron radiation from the same region of the jet, we refer to the process as “synchrotron self-Compton” (SSC) emission. In this case, we can apply the same analysis as in Sect. 4.4 to obtain the flux density at photon energy  $h\nu$  in keV, where  $h$  is Planck’s constant:

$$\begin{aligned}
 F_{\nu}^{\text{SSC}} &\approx c_{\text{SSC}} (h\nu)_{\text{keV}}^{-\alpha} \Theta_{\text{mas}}^{-2(3+2\alpha)} \nu_{\text{m, GHz}}^{-(5+3\alpha)} F_{\text{m, Jy}}^{2(2+\alpha)} \left(\frac{1+z}{\delta}\right)^{2(2+\alpha)} \ln\left(\frac{\nu_{\text{max}}}{\nu_{\text{m}}}\right) \mu\text{Jy} \\
 &\approx (c_{\text{tc}} T_{\text{m, 11}})^{3+2\alpha} (h\nu)_{\text{keV}}^{-\alpha} F_{\text{m, Jy}} \nu_{\text{m, GHz}}^{1+\alpha} \left(\frac{1+z}{\delta}\right)^{2(2+\alpha)} \times \\
 &\quad \ln\left(\frac{\nu_{\text{max}}}{\nu_{\text{m}}}\right) \mu\text{Jy}.
 \end{aligned} \tag{26}$$

The value of  $c_{\text{SSC}}$  is 130, 43, 18, and 91 and that of  $c_{\text{tc}}$  is 0.22, 0.14, 0.11, and 0.083 for  $\alpha = 0.25, 0.5, 0.75,$  and  $1.0,$  respectively. The formula applies over the frequency range  $\sim \gamma_{\text{min}}^2 \nu_{\text{m}}$  to  $\sim \gamma_{\text{max}}^2 \nu_{\text{max}}$  over which the SSC spectrum is a power law with slope  $-\alpha$ . Here,  $\nu_{\text{max}}$  is the highest frequency at which the synchrotron spectrum possesses a power-law slope of  $-\alpha$ .

A simpler formula relates the SSC flux density at frequency  $\nu^{\text{c}}$  to the synchrotron flux density at frequency  $\nu^{\text{s}}$ :

$$\frac{F_{\nu}^{\text{c}}(\nu^{\text{c}})}{F_{\nu}^{\text{s}}(\nu^{\text{s}})} \approx c_{\text{cs}}(\alpha) R N_0 \ln \frac{\nu_2}{\nu_{\text{m}}} \left(\frac{\nu^{\text{s}}}{\nu^{\text{c}}}\right)^{\alpha}, \tag{27}$$

where  $c_{\text{cs}}(\alpha) = 2.7 \times 10^{-22}$ ,  $3.2 \times 10^{-19}$ ,  $3.9 \times 10^{-16}$ ,  $5.0 \times 10^{-13}$  for  $\alpha = 0.25$ ,  $0.5$ ,  $0.75$ , and  $1.0$ , respectively.

The source of seed photons that are scattered may also lie outside the jet or in some other section of the jet. If the seed photons are monochromatic with frequency  $\nu_{\text{seed}}$  and energy density  $u_{\text{seed}}$ , both measured in the rest frame of the host galaxy, the “external Compton” flux density is given by

$$F_{\nu}^{\text{ec}} = c_{\text{ec}}(\alpha) \frac{u_{\text{seed}}}{\nu_{\text{seed}}} D_l^{-2} N_0 f V \delta^{4+2\alpha} (1+z)^{1-\alpha} \left( \frac{\nu_{\text{seed}}}{\nu_{\text{ec}}} \right)^{\alpha}, \quad (28)$$

where  $c_{\text{ec}}(\alpha) \equiv (c\sigma_t/2)(mc^2)^{-2\alpha}$ , with  $\sigma_t$  being the Thomson cross-section, is tabulated in [41]. If the seed photon distribution is actually a Planck function, as is the case for the cosmic microwave background [CMB,  $u_{\text{seed}} = 4.2 \times 10^{-13}(1+z)^4$ ], we can use the same expression if we multiply it by  $c_{\text{planck}}(\alpha) = 0.46, 0.58, 0.75$ , and  $1.00$  for  $\alpha = 0.25, 0.5, 0.75$ , and  $1.0$ , respectively. Since the CMB seed photons are only of relative importance in extended jets and lobes, we express the EC/CMB flux density in units appropriate to the larger scales:

$$F_{\nu}^{\text{ec}}(\text{CMB}) = \frac{c_{\text{cmb}}(\alpha) A f}{1+k} g(\alpha, \gamma_{\text{min}}, \gamma_{\text{max}})^{-1} D_{\text{Gpc}}^3 \Theta_{\text{as}}^3 B_{\mu\text{G}}^2 \delta^{4+2\alpha} \times \\ (1+z)^{-2} (h\nu_{\text{ec}})_{\text{keV}}^{-\alpha} \text{ nJy}, \quad (29)$$

where  $c_{\text{cmb}}(\alpha) \equiv 0.063(4.2 \times 10^6)^{-\alpha} c_{\text{planck}}(\alpha) = 6.4 \times 10^{-4}$ ,  $1.8 \times 10^{-5}$ ,  $5.1 \times 10^{-7}$ ,  $1.5 \times 10^{-8}$  for  $\alpha = 0.25, 0.5, 0.75$ , and  $1.0$ , respectively.

#### 4.6 Matter Content

A major, yet unsettled question is whether jet plasmas are composed of “normal matter”—electrons and protons—electrons and positrons, or a combination of the two. Theoretically, a jet (or sheath of a jet) produced by a wind blown off the accretion disk should contain mainly normal matter. However, in jets that are Poynting flux dominated might be populated by electron-positron pairs created by interaction of high-energy photons with the electromagnetic fields or particles in the jet.

While direct detection of the 511 keV electron-positron two-photon annihilation line would be the strongest evidence for a pair plasma, this emission line is difficult to detect. One of the problems is that current detectors at this energy are relatively insensitive. Another is the relatively low cross-section for annihilation, so that a strong line requires a density higher than that found in jets. In addition, the line width from such a high-velocity environment as a jet flow can cause the line to be broadened beyond recognition. If the jet material mixes with interstellar clouds, however, the positrons can become thermalized and annihilate with cold electrons, leading to a narrow line. This might be occurring in the radio galaxy 3C 120, but even in this case observations have failed thus far to detect a significant spectral feature at the expected energy [63].

Interpretation of circular polarization in the core of the quasar 3C 279 suggests that the jet in this extreme blazar ( $\Gamma > 20$ ; [42]) contains a 5:1 ratio of positrons to protons [82]. This relies on explaining the circular polarization as conversion of linear to circular polarization in an optically thick region. Tuning of the amount of Faraday rotation versus synchrotron self-absorption sets the ratio of positive particle type. However, there has been a suggestion [73] that a suitably turbulent magnetic field in a 100% normal-matter plasma could also reproduce the data.

Various other attempts to determine the matter content are less direct, and have led to contradictory conclusions [18, 72, 75, 17].

## 5 AGN Jets in Context

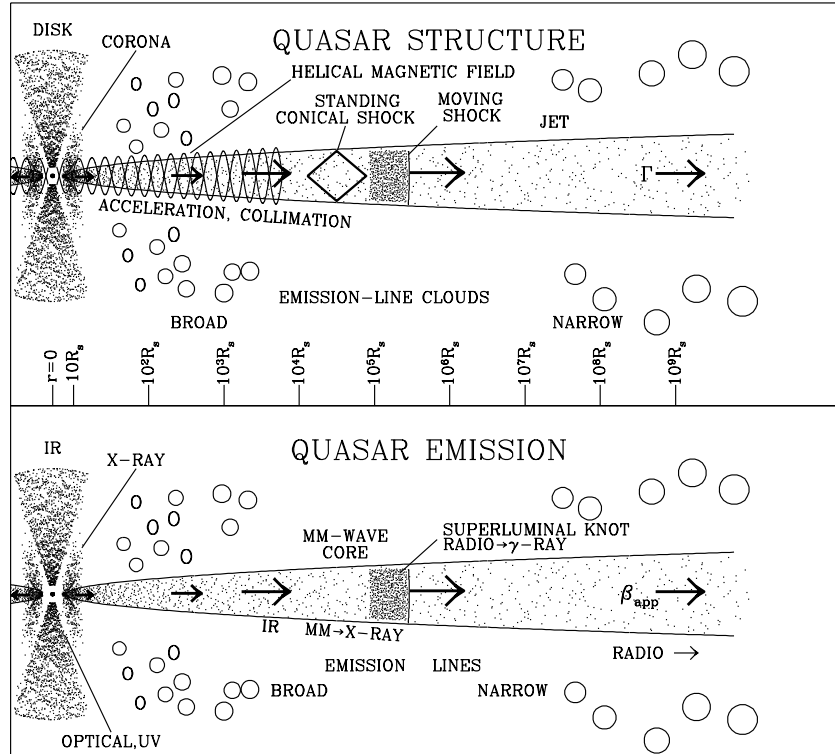
Although only a minority of AGN possess bright, relativistic jets, jets play an important role wherever they are present. A high fraction of the mass-energy accreted onto the black hole can be transformed into highly collimated, high-speed outflows in the form of both jets and winds. This probably stems from the difficulty in squeezing magnetic fields and matter with angular momentum into small spaces, so plasma squirts out perpendicular to the plane of accretion. We do not yet understand the physical conditions that decide whether or not relativistic jets form. The main hint that nature provides is that it seems to be quite difficult in spiral galaxies, but no generally accepted solution has yet grown out of this clue.

Figure 9 sketches the entire AGN system as we currently understand it. The broad-line clouds are immersed in a more dilute, hotter medium, perhaps in a wind emanating from the accretion disk. The jet can be thought of as either the same general outflow, with the velocity increasing toward smaller angles to the polar axes of the disk. Alternatively, the jet is a distinct flow structure that originates in the ergosphere of the black hole, surrounded by the wind but with properties quite different. For example, the jet could be populated mainly by electron-positron pairs, with normal electron-proton plasma representing a minority of the particles.

Our observational tools for probing jets continue to become more sophisticated with time. Millimeter-wave antennas in high-Earth orbit as part of a VLBI array can provide the angular resolution needed to explore regions upstream of the core. Well-sampled multiwaveband flux and, where possible, polarization monitoring observations from radio to  $\gamma$ -ray frequencies might reveal the structure of the jet between these locations and the black hole. And the ever-surprising blazar jets are likely to provide us with singular events that unveil yet another clue in our quest to understand this exotic and enigmatic phenomenon.

## References

1. A. Alberdi, J.M. Marcaide, A.P. Marscher et al: *Astrophys. J.* **402**, 160 (1993)
2. M.F. Aller, H.D. Aller, P.A. Hughes: *Astrophys. J.* **586**, 33 (2003)
3. D.J. Axon, A. Pedlar, S.W. Unger et al: *Nature* **341**, 631 (1989)
4. J.N. Bahcall, S. Kirhakos, D.P. Schneider et al: *Astrophys. J.* **452**, L91 (1995)
5. M.C. Begelman: *Astrophys. J.* **493**, 291 (1998)
6. M.C. Begelman, R.D. Blandford, M.J. Rees: *Rev. Mod. Phys.* **56**, 255 (1984)
7. A.R. Bell: *Mon. Not. Royal Astron. Soc.* **182**, 147 (1978)
8. G.V. Bicknell: *Astrophys. J.* **422**, 542 (1994)
9. R.D. Blandford, A. Königl: *Astrophys. J.* **232**, 34 (1979)
10. R.D. Blandford, A. Levinson: *Astrophys. J.* **441**, 79 (1995)
11. R.D. Blandford, M.J. Rees: *Mon. Not. Royal Astron. Soc.* **169**, 395 (1974)
12. S. Bogovalov, K. Tsinganos: *Mon. Not. Royal Astron. Soc.* **357**, 918 (2005)
13. A.H. Bridle: *Astron. J.* **89**, 979 (1984)



**Fig. 9.** Cartoon illustrating the various physical and emission components of a quasar or other AGN with a relativistic jet. The length scale (shown along the bottom of the top panel in terms of Schwarzschild radii of the black hole) is logarithmic in order to include phenomena over a wide range of distances from the black hole. The radiation produced in the jet is relativistically beamed, while that outside the jet is not

14. G.R. Burbidge: *Astrophys. J.* **129**, 849 (1959)
15. B.J. Burn: *Mon. Not. Royal Astron. Soc.* **133**, 67 (1966)
16. T.V. Cawthorne: *Mon. Not. Royal Astron. Soc.* **367**, 851 (2006)
17. A. Celotti: *Astrophys. Space Sci.* **288**, 175 (2003)
18. A. Celotti, A.C. Fabian: *Mon. Not. Royal Astron. Soc.* **264**, 228 (1993)
19. C.C. Cheung, D.E. Harris, L. Stawarz: *Astrophys. J.* **663**, L65 (2007)
20. W.D. Cotton, J.J. Wittels, I.I. Shapiro et al: *Astrophys. J.* **238**, L123 (1980)
21. R. Courant, K.O. Friedrichs: *Supersonic Flow and Shock Waves* (Springer-Verlag, New York Berlin Heidelberg London Paris Tokyo Hong Kong Barcelona Budapest 1948)
22. R.A. Daly, A.P. Marscher: *Astrophys. J.* **334**, 539 (1988)
23. F.D. D’Arcangelo, A.P. Marscher, S.G. Jorstad et al: *Astrophys. J.* **659**, L107
24. D.S. De Young: *The Physics of Extragalactic Radio Sources* (The University of Chicago Press, Chicago 2002)
25. E. Fermi: 1949, *Phys. Rev.* **75**, 1169 (1949)

26. H.C. Ford, R.J. Harms, Z.I. Tsvetanov et al: *Astrophys. J.* **435**, L27 (1994)
27. J.L. Gómez, J.M. Martí, A.P. Marscher et al: *Astrophys. J.* **449**, L19 (1995)
28. J.L. Gómez, A.P. Marscher, A. Alberdi et al: *Science* **289**, 2317 (2000)
29. P.E. Hardee: AGN Jets: A Review of Stability and Structure. In: *Relativistic Jets: The Common Physics of AGN, Microquasars, and Gamma-Ray Bursts*, AIP Conf. Proc., vol 856, ed by P.A. Hughes, J.N. Bregman, (American Institute of Physics, Melville, New York 2006), pp 57–77
30. R.J. Harms, H.C. Ford, Z.I. Tsvetanov et al: *Astrophys. J.* **435**, L35 (1994)
31. R.C. Hartman, D.L. Bertsch, S.D. Bloom et al: *Astrophys. J. Suppl.* **123**, 79 (1999)
32. J. Hawley, J.H. Krolik: *Astrophys. J.* **641**, 103 (2006)
33. D.C. Homan, Y.Y. Kovalev, M.L. Lister et al: *Astrophys. J.* **642**, 115 (2006)
34. C.T. Hua: *Astron. J.* **199**, 105 (1988)
35. P.A. Hughes, ed: *Beams and Jets in Astrophysics* (Cambridge University Press, Cambridge New York Port Chester Melbourne Sydney 1991)
36. P.A. Hughes, H.D. Aller, M.F. Aller: *Astrophys. J.* **298**, 301 (1985)
37. P.A. Hughes, H.D. Aller, M.F. Aller: *Astrophys. J.* **341**, 54 (1989)
38. C. Impey, G. Neugebauer: *Astron. J.* **95**, 307 (1988)
39. T.W. Jones, S.L. Odell: *Astrophys. J.* **214**, 522 (1977)
40. S.G. Jorstad, A.P. Marscher, J.R. Mattox: *Astrophys. J. Suppl.* **134**, 181 (2001)
41. S.G. Jorstad, A.P. Marscher: *Astrophys. J.* **614**, 615 (2004)
42. S.G. Jorstad, A.P. Marscher, M.L. Lister et al: *Astron. J.* **130**, 1418 (2005)
43. W. Junor, J.A. Biretta, M. Livio: *Nature*, **401**, 891 (1999)
44. J. Kataoka, J.R. Mattox, J. Quinn: *Astrophys. J.* **514**, 138 (1999)
45. Kellermann, K. I., M.L. Lister, D.C. Homan et al: *Astrophys. J.* **609**, 539 (2004)
46. A. Königl: *Astrophys. J.* **243**, 700 (1981)
47. Y.Y. Kovalev, K.I. Kellermann, M.L. Lister et al: *Astron. J.* **130**, 2473
48. J.H. Krolik: *Active Galactic Nuclei* (Princeton University Press Princeton)
49. R.A. Laing: Brightness and Polarization Structure of Decelerating Relativistic Jets: in *Energy Transportation in Galaxies and Quasars*, ASP Conf. Ser., vol 100, ed by P.E. Hardee, A.H. Bridle, J.A. Zensus (Astronomical Society of the Pacific, San Francisco 1996), pp. 241–252
50. R.A. Laing, A.H. Bridle: *Mon. Not. Royal Astron. Soc.* **336**, 328 (2002)
51. R.A. Laing, J.R. Canvin, A.H. Bridle: *Astronomische Nachrichten* **327**, 523
52. R.A. Laing, P. Parma, H.R. de Ruiter et al: *Mon. Not. Royal Astron. Soc.* **306**, 513 (1999)
53. M.L. Lister, D.C. Homan: *Astron. J.* **130**, 1389
54. A.P. Lobanov: *Astron. Astrophys.* **330**, 79 (1998)
55. F.D. Macchetto, A. Marconi, D.J. Axon et al: *Astrophys. J.* **489**, 579 (1997)
56. A.P. Marscher: *Astrophys. J.* **235**, 386 (1980)
57. A.P. Marscher: *Astrophys. J.* **264**, 296 (1983)
58. A.P. Marscher: Synchro-Compton Emission from Superluminal Sources. In: *Superluminal Radio Sources*, ed by J.A. Zensus, T.J. Pearson (Cambridge Univ. Press, Cambridge 1987), pp 280–300
59. A.P. Marscher: *Proc. Nat. Acad. Sci.* **92**, 11439 (1995)
60. A.P. Marscher, W.K. Gear: *Astrophys. J.* **298**, 114 (1985)
61. A.P. Marscher, W.K. Gear, J.P. Travis: Variability of Nonthermal Continuum Emission in Blazars. In: *Variability of Blazars*, ed by E. Valtaoja, M. Valtonen (Cambridge Univ. Press, Cambridge 1992), pp 85–101

62. A.P. Marscher, S.G. Jorstad, J.L. Gómez et al: *Nature* **417**, 625 (2002)
63. A.P. Marscher, S.G. Jorstad, J.L. Gómez et al: *Astrophys. J.* **665**, 232 (2007)
64. J.C. McKinney, R. Narayan: *Mon. Not. R. Astron. Soc.* **375**, 531 (2007)
65. D.L. Meier, S. Koide, Y. Uchida: *Science* **291**, 84 (2000)
66. R. Mittal, R. Porcas, O. Wucknitz et al: *Astron. Astrophys.* **447**, 515 (2006)
67. A. Pacholczyk: *Radio Astrophysics* (Freeman, San Francisco 1970)
68. R.A. Perley, J.W. Dreher, J.J. Cowan: *Astrophys. J.* **285**, L35 (1984)
69. B. Punsley: *Astrophys. J.* **473**, 178 (1996)
70. A.B. Pushkarev, D.C. Gabuzda, Yu.N. Vetukhnovskaya et al: *Mon. Not. R. Astron. Soc.* **356** 859 (2005)
71. A.C.S. Readhead: *Astrophys. J.* **426**, 51 (1994)
72. C.S. Reynolds, A.C. Fabian, A. Celotti et al: *Mon. Not. Royal Astron. Soc.* **283**, 873 (1996)
73. M. Ruszkowski, M.C. Begelman: *Astrophys. J.* **573**, 485 (2002)
74. M. Sikora, M.C. Begelman, G.M. Madejski, et al: *Astrophys. J.* **625**, 72 (2005)
75. M. Sikora, G. Madejski: *Astrophys. J.* **534**, 109 (2000)
76. H. Sol, G. Pelletier, E. Asséo: *Mon. Not. R. Astron. Soc.* **237**, 411 (1989)
77. M. Türlér, T.J.-L. Courvoisier, S. Paltani: *Astron. Astrophys.* **349**, 45 (1999)
78. M. Türlér, T.J.-L. Courvoisier, S. Paltani: *Astron. Astrophys.* **361**, 850 (2000)
79. N. Vlahakis: Disk-Jet Connection. In: *Blazar Variability Workshop II: Entering the GLAST Era*, Astronomical Society of the Pacific Conf. Ser., vol 350, ed by H.R. Miller, K. Marshall, J.R. Webb et al, (Astron. Soc. Pacific, San Francisco 2006), pp 169–177
80. N. Vlahakis, A. Königl: *Astrophys. J.* **605**, 656 (2004)
81. R.C. Walker, J.M. Benson, S.C. Unwin: *Astrophys. J.* **316**, 546 (1987)
82. J.F.C. Wardle, D.C. Homan, R. Ojha et al: *Nature* **395**, 457 (1998)